

Modeling of the Stress- and Magnetic Field-Induced Variant Reorientation in MSMA

Bjoern Kiefer* and Dimitris C. Lagoudas†

Texas A&M University, College Station, TX, 77843-3141, USA

This paper is concerned with the modeling of the magnetic shape memory alloy (MSMA) constitutive response caused by the reorientation of martensitic variants. Following a summary of the constitutive model previously proposed by the authors, the nonlinear and hysteretic strain and magnetization response of MSMA are investigated for two main loading cases, namely the magnetic field-induced reorientation of variants under constant uniaxial stress and the stress-induced reorientation under constant magnetic field. It is demonstrated in this work that the model captures the loading history dependence of the constitutive behavior through the evolution of internal state variables. Complex loading cases are also presented in which the sequence of the application of the stress and magnetic field strongly influences the predicted response. The relation of critical stresses and magnetic fields for the activation of the reorientation process are visualized in a variant reorientation diagram on which the considered loading paths are superimposed.

I. Introduction

Due to their ability to produce recoverable magnetic field-induced strains at least one order of magnitude higher than those of ordinary magnetostrictive or piezomagnetic materials, magnetic shape memory alloys have intensely been researched since the first studies of their behavior were reported by Ullakko et al.,¹ who found magnetic field-induced strains of nearly 0.2% in stress-free experiments on martensitic NiMnGa single crystals. Extensive experimental work on single crystals of off-stoichiometric intermetallic compounds near the composition Ni₂MnGa have yielded strains of up to 10%.² Other alloys have been investigated, such as FePd,^{3,4} FeNiCoTi⁵ and CoNiAl.⁶ In addition to the large recoverable strains, which are caused by the field-driven reorientation of martensitic variants, magnetic shape memory alloys are characterized by the nonlinear and hysteretic nature of their response, as well as the coupling of the shape change and the nonlinear change in the magnetization.

MSMA are attractive materials for actuator and sensor design,^{7,8} which are particularly important for aerospace applications. Examples of applications of smart structures technology in which shape memory alloys (SMAs) have been employed include rotorcraft systems^{9,10} and SMA actuated reconfigurable wings.¹¹ Magnetic shape memory alloys actuators, which have now become commercially available on a limited scale,¹² exhibit a greater actuation bandwidth than conventional shape memory alloys, because their actuation frequency is not limited by heat transfer. They may therefore replace SMA actuators in certain future applications. In the design process of MSMA actuators, it is inevitable that the intrinsic coupling between mechanical and magnetic effects in these materials be addressed. A reliable constitutive model for numerical analysis is needed as a tool in the development process to go beyond trial-and-error development techniques involving extensive experimental testing.

Several constitutive models for MSMA have been proposed in the literature.¹³⁻¹⁷ Most of these formulations rely on the minimization of a free energy expression, which searches for equilibrium points in ideal processes. This paper and previous work by the authors,¹⁸⁻²¹ however, is concerned with the influence of dissipative effects on the evolution of thermodynamic states and thus the loading history dependence of

*Ph.D. Candidate and Graduate Assistant Research, Department of Aerospace Engineering, Texas A&M University, H.R. Bright Building, 3141 TAMU, College Station, TX 77843-3141, AIAA Student Member.

†John and Bea Slattery Chair, Department of Aerospace Engineering, Texas A&M University, H.R. Bright Building, 3141 TAMU, College Station, TX 77843-3141, AIAA Associate Fellow.

the constitutive response; an approach that has yielded powerful phenomenological models for conventional shape memory alloys.^{22,23}

The most commonly investigated MSMA is NiMnGa, in which the 5M (five-layered modulated) martensite^{24,25} consists of three tetragonal variants. If in the martensitic phase a uniaxial compressive stress and a perpendicular magnetic field are applied along the appropriate crystallographic directions, one variant is stress-favored, one magnetic field-favored and the third variant is eliminated. This competing influence of mechanical and magnetic loads in a two variant setup is the focus of the modeling efforts in this paper. Two main loading cases are considered: i) variable magnetic field under constant stress; ii) variable stress under constant magnetic field. The term magnetic field-induced strain (MFIS) will be used only if the variant reorientation is solely driven by the magnetic field, otherwise the more general term reorientation strain will be employed. Furthermore, the influence of the history of magnetomechanical loading on the constitutive response is investigated by varying the order in which the stress and the magnetic field are varied. A variant reorientation diagram is proposed to be used as a modeling tool that can provide great insight into the expected material response under complex loading paths.

Section II presents a summary of the MSMA constitutive model equations. Section III deals with the reduction of the model for special loading cases as well as the calibration of model parameters and presents the predicted constitutive response, which is discussed in detail. The paper concludes with a discussion of the presented results and an outlook on future modeling efforts in Section IV.

II. MSMA Constitutive Equations

In this section a summary of the framework for the MSMA constitutive model previously proposed by the authors¹⁸⁻²⁰ is given. The model is concerned with the stress and magnetic field-induced rearrangement of martensitic variants and predicts the associated nonlinear, stress-dependent reorientation strain and magnetization hysteresis curves typically observed in experiments.^{26,26-28} For the loading case of variable magnetic field and constant uniaxial stress, such experimental data, taken from the literature, is presented in Section III, cf. figure 2(a) on page 7 and figure 3 on page 10, in the context of validating the constitutive model predictions.

The approach is based on the formulation of a Gibbs free energy function G , in which the stress $\boldsymbol{\sigma}$ and the magnetic field strength \mathbf{H} are the independent state variables. The constitutive equations for the dependent state variables, namely the elastic strain $\boldsymbol{\varepsilon}^e$ and the magnetization \mathbf{M} , are derived by taking partial derivatives of the free energy function; a procedure that is consistent with thermodynamic restrictions and follows the methodology of Coleman and Noll.^{29,30} Dissipative effects associated with twin boundary or magnetic domain wall motion, which are reflected in the macroscopically observed hysteretic nature of the material response, are taken into account by a set of internal state variables. The evolution of these internal state variables captures the loading history dependence of the constitutive response. Motivated by microstructural observations^{31,32} the martensitic variant volume fraction ξ , the magnetic domain volume fraction α and the angles between the magnetization vectors and the magnetic easy axes in each domain, are chosen as the appropriate set of internal state variables. To keep the formulation simple, cases are considered in which, through proper initial stress application, only two martensitic variants coexist. The nomenclature is such that the volume fraction of the compressive stress-favored variant 1 is denoted ξ , while accordingly that of the perpendicular magnetic field-favored variant 2 is $1 - \xi$.

The energy terms that have been identified as relevant for the magnetic shape memory effect and therefore contribute to the free energy expression are the elastic strain energy, the Zeeman energy and the magnetocrystalline anisotropy energy. The Zeeman or external field energy^{33,34} aims to align the local magnetization with the applied magnetic field. The magnetocrystalline or short magnetic anisotropy energy can be viewed as the energy stored in the material due to the work done by an applied field in rotating the magnetization away from the magnetic easy axes.^{35,36} Accordingly, the specific form of the Gibbs free energy for the Kiefer and Lagoudas model¹⁹ is given by

$$\begin{aligned} G &= \hat{G}(\boldsymbol{\sigma}, \mathbf{H}, \xi, \alpha, \theta_i) \\ &= -\frac{1}{2\rho} \boldsymbol{\sigma} : \mathcal{S}(\xi) \boldsymbol{\sigma} - \frac{\mu_0}{\rho} \mathbf{M}^{\text{eff}}(\xi, \alpha, \theta_i) \cdot \mathbf{H} + G^{\text{an}}(\xi, \alpha, \theta_i) + G^{\text{mix}} + G_0, \end{aligned} \quad (1)$$

where ρ is the mass density and μ_0 is the permeability of free space. The effective elastic compliance \mathcal{S} ,

effective magnetization \mathbf{M}^{eff} and effective magnetic anisotropy energy G^{an} are defined as

$$\mathcal{S} := (1 - \xi)\mathcal{S}^{\text{V}_1} + \xi\mathcal{S}^{\text{V}_2} = \mathcal{S}^{\text{V}_1} + \xi\Delta\mathcal{S}, \quad \Delta\mathcal{S} := \mathcal{S}^{\text{V}_2} - \mathcal{S}^{\text{V}_1}; \quad (2a)$$

$$\begin{aligned} \mathbf{M}^{\text{eff}} &:= (1 - \xi)\mathbf{M}^{\text{V}_1} + \xi\mathbf{M}^{\text{V}_2} \\ &= (1 - \xi)[(1 - \alpha)\mathbf{M}^1(\theta_1) + \alpha\mathbf{M}^3(\theta_3)] + \xi[(1 - \alpha)\mathbf{M}^2(\theta_2) + \alpha\mathbf{M}^4(\theta_4)]; \end{aligned} \quad (2b)$$

$$\begin{aligned} G^{\text{an}} &:= (1 - \xi)G^{\text{an,V}_1} + \xi G^{\text{an,V}_2} \\ &= (1 - \xi)[(1 - \alpha)G^{\text{an,1}}(\theta_1) + \alpha G^{\text{an,3}}(\theta_3)] + \xi[(1 - \alpha)G^{\text{an,2}}(\theta_2) + \alpha G^{\text{an,4}}(\theta_4)], \end{aligned} \quad (2c)$$

where the magnetization vectors \mathbf{M}^i are defined as

$$\begin{aligned} \mathbf{M}^1 &:= -M^{\text{sat}}(\cos(\theta_1)\mathbf{e}_x + \sin(\theta_1)\mathbf{e}_y), & \mathbf{M}^2 &:= M^{\text{sat}}(\sin(\theta_2)\mathbf{e}_x - \cos(\theta_2)\mathbf{e}_y), \\ \mathbf{M}^3 &:= M^{\text{sat}}(\cos(\theta_3)\mathbf{e}_x + \sin(\theta_3)\mathbf{e}_y), & \mathbf{M}^4 &:= M^{\text{sat}}(-\sin(\theta_4)\mathbf{e}_x + \cos(\theta_4)\mathbf{e}_y). \end{aligned} \quad (3)$$

G^{mix} is a mixing term¹⁹ and G_0 is the reference state value of the Gibbs free energy. The anisotropy energy contributions by the individual magnetic domains $G^{\text{an},i}$ can, for an assumed uniaxial symmetry, be expressed as a series expansion of the form³⁷

$$G^{\text{an},i} = \sum_{n=1}^N K_n \sin^{2n}(\theta), \quad (4)$$

of which only the first term will be considered in the current model.

The evolution of internal state variables must satisfy the second law of thermodynamics in form of the Clausius-Duhem inequality, which in this case can be written as¹⁹

$$\pi^\xi \dot{\xi} + \sum_i^4 \pi^{\theta_i} \dot{\theta}_i \geq 0. \quad (5)$$

From physical observations it is reasonable to assume that the rotation of the magnetization vectors away from the magnetic easy axes is a thermodynamically reversible process.^{35,37} According to Eq. (5) this implies that the driving force for dissipative processes associated with the evolution of the rotation angles must vanish^a, i. e.

$$\pi^{\theta_i} := -\rho \frac{\partial \hat{G}}{\partial \theta_i} \equiv 0. \quad (6)$$

These constraints will be utilized to eliminate the explicit dependence of the constitutive equations on the rotation angles θ_i .

The evolution of magnetic domains, although accounted for in the general modeling framework, has been neglected in this paper. This simplification is based on the idea that unfavorable domains are eliminated at relatively low fields,^{2,38} such that they do not significantly influence the magnetic field-induced variant reorientation process. In Section III.A the validity of this assumption will be evaluated by comparing predicted magnetization curve with experimental data. For the case of fixed magnetic domain structure, the driving force π^α need not be considered. The domain volume fraction in this case takes the value of $\alpha = 1$, for $H_y > 0$, and $\alpha = 0$ for $H_y < 0$, which leads to simplified forms of the expressions (1), (2b).

The remaining equations for the rate-independent MSMA constitutive model are summarized in table 1 on the following page. For more detail the reader is referred to earlier publications by the authors.^{19,20} Explicit forms of the expressions $\varepsilon(\boldsymbol{\sigma}, \mathbf{H}, \xi)$, $\mathbf{M}(\boldsymbol{\sigma}, \mathbf{H}, \xi)$ and $\pi^\xi(\boldsymbol{\sigma}, \mathbf{H}, \xi)$ will be given in the following section in which the presented model equations are reduced for the two discussed loading cases.

^aTo avoid misunderstanding, this does not mean that the rotation angles are fixed, but rather that no dissipation is associated with the rotation of the magnetization.

Table 1. Summary of the equations for the Kiefer and Lagoudas MSMA constitutive model.

<p>Strain and Magnetization:</p> $\boldsymbol{\varepsilon} = \boldsymbol{\varepsilon}^e + \boldsymbol{\varepsilon}^r + \bar{\boldsymbol{\varepsilon}}^{\text{off}}, \quad \boldsymbol{\varepsilon}^e := -\rho \frac{\partial \hat{G}}{\partial \boldsymbol{\sigma}}, \quad \dot{\boldsymbol{\varepsilon}}^r = \boldsymbol{\Lambda}^r \dot{\xi}.$ $\mathbf{M} := -\frac{\rho}{\mu_0} \frac{\partial \hat{G}}{\partial \mathbf{H}},$ <p>Driving Forces for Variant Reorientation and Magnetization Rotation</p> $\pi^\xi := \boldsymbol{\sigma} : \boldsymbol{\Lambda}^r - \rho \frac{\partial \hat{G}}{\partial \xi}, \quad \pi^{\theta_i} := -\rho \frac{\partial \hat{G}}{\partial \theta_i}.$ <p>Reorientation Function:</p> $\Phi^\xi(\boldsymbol{\sigma}, \mathbf{H}, \xi) = \begin{cases} \pi^\xi - Y^{\xi,c}, & \dot{\xi} > 0 \\ -\pi^\xi - Y^{\xi,c}, & \dot{\xi} < 0 \end{cases}.$ <p>Kuhn-Tucker Loading Conditions:</p> $\Phi^\xi(\boldsymbol{\sigma}, \mathbf{H}, \xi) \leq 0, \quad \Phi^\xi \dot{\xi} = 0.$ <p>Trigonometric Hardening Function:</p> $f^{\xi,c} = \rho G^{\text{mix}}; \quad \frac{\partial f^{\xi,c}}{\partial \xi} = \begin{cases} -A^c [\pi - \cos^{-1}(2\xi - 1)] + (B_1^c + B_2^c), & \dot{\xi} > 0 \\ -C^c [\pi - \cos^{-1}(2\xi - 1)] + (B_1^c - B_2^c), & \dot{\xi} < 0 \end{cases}.$

III. MSMA Response under Specific Magnetomechanical Loading Paths.

A. Variant reorientation under a variable magnetic field transverse to a constant uniaxial stress.

1. Reduced model equations

First, the most common loading case is considered in which the MSMA is subjected to different levels of constant compressive uniaxial stress (x -direction) and a variable magnetic field perpendicular to the mechanical load (y -direction)^b.

Following the discussion of Section II, it is assumed that the magnetic domain volume fraction is fixed and switches from $\alpha = 1$ to $\alpha = 0$ when the applied magnetic field switches sign. All of the reduced equations presented in this section are derived for the case of $\alpha = 1$.^c For the chosen coordinate system, the non-zero components of the reorientation strain tensor are given by $\Lambda_{11}^r = -\Lambda_{22}^r = \varepsilon^{r,\text{max}}$. The maximum strain value can be measured experimentally or is often approximated as $\varepsilon^{r,\text{max}} = (a - c)/a$, where a and c are the lattice parameters of martensite. Reorientation strain tensors for arbitrary single crystal orientations have been discussed in the literature.^{4,24,39}

With the Gibbs free energy given by Eq. (1) and utilizing the specified simplifications, the constraint (6) for θ_3 takes the form

$$\pi^{\theta_3} := -\rho \frac{\partial \hat{G}}{\partial \theta_3} = (1 - \xi) [\mu_0 M^{\text{sat}} H_y - 2\rho K_1 \sin(\theta_3)] \cos(\theta_3) = 0, \quad (7)$$

^bThe coordinate system is chosen such that its directions align with the $\langle 100 \rangle_{\text{m}}$ -directions of the considered 5M tetragonal martensite.

^cSince all equations in Section II were specified for the general case, it is straightforward to derive their counterparts for $\alpha = 0$.

which leads to

$$\sin(\theta_3) = \frac{\mu_0 M^{\text{sat}}}{2\rho K_1} H_y, \quad (8)$$

for $0 \leq \theta_3 < \frac{\pi}{2}$ and $0 \leq \xi < 1$. Since the easy axis of variant 2 is aligned with the direction of the applied field, its magnetization vector does not rotate, such that the corresponding constraint $\pi^{\theta_4} = 0$ is identically satisfied.

For the considered loading case and using constraint (8), the driving force for variant rearrangement reduces to

$$\pi^\xi = \sigma \varepsilon^{r,\max} + \mu_0 M^{\text{sat}} H_y - \frac{(\mu_0 M^{\text{sat}})^2}{4\rho K_1} H_y^2 - \frac{\partial f^\xi}{\partial \xi}, \quad (9)$$

where $\frac{\partial f^\xi}{\partial \xi}$ has been specified in table 1 and the difference in the elastic compliance of the variants $\Delta \mathcal{S}$ has been neglected. By enforcing the Kuhn-Tucker loading conditions and using the reorientation function of table 1 on the previous page in combination with the driving force expression (9), the evolution equations for the martensitic variant volume fraction ξ are derived as follows:

For the forward reorientation process (Variant 1 \rightarrow Variant 2, $\dot{\xi} > 0$):

$$\begin{aligned} \Phi^\xi \dot{\xi} = 0 &\Rightarrow \Phi^\xi = 0 \Rightarrow \pi^\xi = Y^{\xi,c}. \\ \pi^\xi = \sigma \varepsilon^{r,\max} + \mu_0 M^{\text{sat}} H_y - \frac{(\mu_0 M^{\text{sat}})^2}{4\rho K_1} H_y^2 + A^c [\pi - \cos^{-1}(2\xi - 1)] - B_1^c - B_2^c &= Y^{\xi,c}. \end{aligned} \quad (10)$$

Due its scalar nature one can solve for ξ in closed-form, which yields

$$\xi^{(1,2)} = \frac{1}{2} \cos \left(-\frac{1}{A^c} \left[-\sigma \varepsilon^{r,\max} - \mu_0 M^{\text{sat}} H_y + \frac{(\mu_0 M^{\text{sat}})^2}{4\rho K_1} H_y^2 + B_1^c + B_2^c + Y^{\xi,c} \right] + \pi \right) + \frac{1}{2}. \quad (11)$$

Similarly it follows for the reverse reorientation process (Variant 2 \rightarrow Variant 1, $\dot{\xi} < 0$):

$$\begin{aligned} \Phi^\xi \dot{\xi} = 0 &\Rightarrow \Phi^\xi = 0 \Rightarrow \pi^\xi = -Y^{\xi,c}. \\ \pi^\xi = \sigma \varepsilon^{r,\max} + \mu_0 M^{\text{sat}} H_y - \frac{(\mu_0 M^{\text{sat}})^2}{4\rho K_1} H_y^2 + C^c [\pi - \cos^{-1}(2\xi - 1)] - B_1^c + B_2^c &= -Y^{\xi,c}, \end{aligned} \quad (12)$$

so that

$$\xi^{(2,1)} = \frac{1}{2} \cos \left(-\frac{1}{C^c} \left[-\sigma \varepsilon^{r,\max} - \mu_0 M^{\text{sat}} H_y + \frac{(\mu_0 M^{\text{sat}})^2}{4\rho K_1} H_y^2 + B_1^c - B_2^c - Y^{\xi,c} \right] + \pi \right) + \frac{1}{2}. \quad (13)$$

For the considered loading case, all the necessary equations have now been derived. The next section discusses the calibration of model parameters.

2. Calibration of the model parameters

The material parameters consist of the magnetic anisotropy constant ρK_1 , the saturation magnetization M^{sat} , the maximum reorientation strain $\varepsilon^{r,\max}$, which follow from standard experiments described in the literature.^{28,40} Additional input are the critical magnetic field values $H_y^{s(1,2)}$, $H_y^{f(1,2)}$, $H_y^{s(2,1)}$ and $H_y^{f(2,1)}$, which denote the onset and termination of the forward and reverse magnetic field-induced reorientation process, respectively. They are experimentally obtained from *one* magnetic field-induced strain hysteresis loop, cf. figure 2(a) on page 7, at the stress level σ^* , which can be arbitrarily chosen in the range between zero and the blocking stress. The general relations between the material and the model parameters are listed in table 2, which have been derived by evaluating the evolution equations for the martensitic variant volume fraction in the forward (11) and reverse (13) reorientation process at $\xi = 0$ and $\xi = \xi^{\text{crit}}$, respectively, and enforcing continuity of the hardening function at $\xi = 1$. ξ^{crit} is the maximum volume fraction of variant 2 obtained at the stress level σ^* , which can be estimated by relating the maximum reorientation strain for this stress level to the maximum achievable reorientation strain $\varepsilon^{r,\max}$. For the case of complete reorientation ξ^{crit} is equal to 1 and the listed relations simplify.

Table 2. Relations between material constants and model parameters.

$$\begin{aligned}
 A^c &= \frac{\mu_0 M^{\text{sat}}}{(\pi - \cos^{-1}(2\xi^{\text{crit}} - 1))} \left(H_y^{s(1,2)} - H_y^{f(1,2)} \right) - \frac{(\mu_0 M^{\text{sat}})^2}{4\pi\rho K_1} \left[\left(H_y^{s(1,2)} \right)^2 - \left(H_y^{f(1,2)} \right)^2 \right] \\
 B_1^c &= \frac{1}{2} \mu_0 M^{\text{sat}} \left(H_y^{s(1,2)} + H_y^{f(2,1)} \right) - \frac{(\mu_0 M^{\text{sat}})^2}{8\rho K_1} \left[\left(H_y^{s(1,2)} \right)^2 + \left(H_y^{f(2,1)} \right)^2 \right] + \sigma^* \varepsilon^{\text{r,max}} \\
 B_2^c &= \frac{\pi}{4} \left(A^c - C^c \right) \\
 C^c &= \frac{\mu_0 M^{\text{sat}}}{(\pi - \cos^{-1}(2\xi^{\text{crit}} - 1))} \left(H_y^{f(2,1)} - H_y^{s(2,1)} \right) - \frac{(\mu_0 M^{\text{sat}})^2}{4\pi\rho K_1} \left[\left(H_y^{f(2,1)} \right)^2 - \left(H_y^{s(2,1)} \right)^2 \right] \\
 Y^{\varepsilon,c} &= \frac{1}{2} \mu_0 M^{\text{sat}} \left(H_y^{s(1,2)} - H_y^{f(2,1)} \right) - \frac{(\mu_0 M^{\text{sat}})^2}{8\rho K_1} \left[\left(H_y^{s(1,2)} \right)^2 - \left(H_y^{f(2,1)} \right)^2 \right] - B_2^c
 \end{aligned}$$

This methodology was employed to obtain the model parameters listed in table 3, which also specifies the material parameters that were extracted from experimental data published by Heczko et al.²⁵ It should be pointed out that, due to the sensitivity and nonlinear nature of the constitutive model, calibrating material parameters can be a tedious effort. Particular calibration strategies and parameters optimization methods can be used to obtain better model parameter sets. However, once the model parameters have been calibrated, all model predictions are performed *without readjusting the parameters*.

Table 3. Material parameters for the considered Ni_{50.7}Mn_{28.4}Ga_{20.9} composition, and the resulting hardening and hysteresis parameters.

Material Parameters			Model Parameters		
Quantity	Value	Unit	Quantity	Value	Unit
ρK_1	167.0	kJm ⁻³	$\mu_0 H_y^{s(1,2)}$	0.2	T
M^{sat}	510.0	kAm ⁻¹	$\mu_0 H_y^{f(1,2)}$	0.32	T
$\varepsilon^{\text{r,max}}$	6.2	%	$\mu_0 H_y^{s(2,1)}$	0.0	T
σ^*	-0.2	MPa	$\mu_0 H_y^{f(2,1)}$	-0.135	T
			A^c	-11.747	kPa
			B_1^c	-7.161	kPa
			B_2^c	9.761	kPa
			C^c	-24.174	kPa
			$Y^{\varepsilon,c}$	71.425	kPa

3. Model predictions

The constitutive model for MSMA has been proposed in Section II, and the constitutive equations have been simplified for the special loading case of constant uniaxial stress and variable transverse magnetic field in Section III.A.1. The model parameters have been calibrated in Section III.A.2. This section presents numerical results for the predicted response for the loading case of variable magnetic field under constant stress.

Before specific response curves are presented, it is helpful to gain more insight into the material response expected under a particular loading path, by consulting a variant reorientation diagram, which is a graphical representation of the stress dependence of the activation fields for the variant reorientation process. Similarly, the visualization of the martensitic phase transformation conditions in phase diagrams is common for conventional shape memory alloys.^{41,42} Figure 1 depicts the numerical variant reorientation diagram for the considered composition in terms of the stress vs. magnetic field. It has been constructed by evaluating the reorientation conditions (10) and (12) at $\xi = 0$ and $\xi = 1$, respectively. A similar reorientation diagram was previously proposed by the authors¹⁹ for an earlier version of the constitutive model, in which the magnetization was assumed to be fixed to the respective magnetic easy axes.

At the stress level of $\sigma^* = -0.2$ MPa, for which the model parameters were calibrated, the loading paths intersects the activation lines, at the critical magnetic field values $H_y^{s(1,2)}(\sigma^*)$, $H_y^{f(1,2)}(\sigma^*)$, $H_y^{s(2,1)}(\sigma^*)$, whose numerical values were specified in Table 3. Note that the value of $H_y^{f(2,1)}(\sigma^*)$ is outside of the physically meaningful region, reflecting the fact that the reverse reorientation process is not completed for the considered stress level. For the model parameter calibration this value was estimated by using the magnitude of the residual strain as additional input. The line at $\mu_0 H^{\text{crit}} = 0.655$ T marks the critical magnetic field at which the

magnetization in both variant has been fully aligned with the applied field, such that the variant reorientation process is terminated. For cases of incomplete reorientation, the appropriate activation lines lie within the regions bounded by the lines for $\xi=0$ and $\xi=1$ depicted in the reorientation diagram.

Several important features can be concluded from the variant reorientation diagram for this particular set of parameters: i) the blocking stress is predicted to be -1.33 MPa; ii) only in the range of 0 to -0.95 MPa is the maximum strain obtained by complete variant reorientation. For higher stress levels the reorientation is only partial; iii) stress levels lower than $|\sigma|=0.2$ MPa are insufficient to induce the recovery of variant 1 when the magnetic field is removed; iv) variant 1 can in fact not be fully recovered under any constant stress level, since the appropriate stress level is above the blocking stress.

Figure 2(a) displays the resulting magnetic field-induced strain curves for several different stress levels. These curves have been computed by utilizing the reorientation conditions (10) and (12), the evolution equations for the variant volume fraction (11) and (13), the proportionality of the reorientation strain and ξ , cf. table 1, and the parameters listed in table 3. Note that for reasons of comparison, the reorientation strain and not the total strain has been plotted in this figure. The curve at -0.2 MPa has to be considered a simulation, since its experimental equivalent was used to obtain the model parameters. The curves at all other stress levels, however, are model predictions. It is again emphasized, that the **same** set of parameters has been used for all of the predictions.

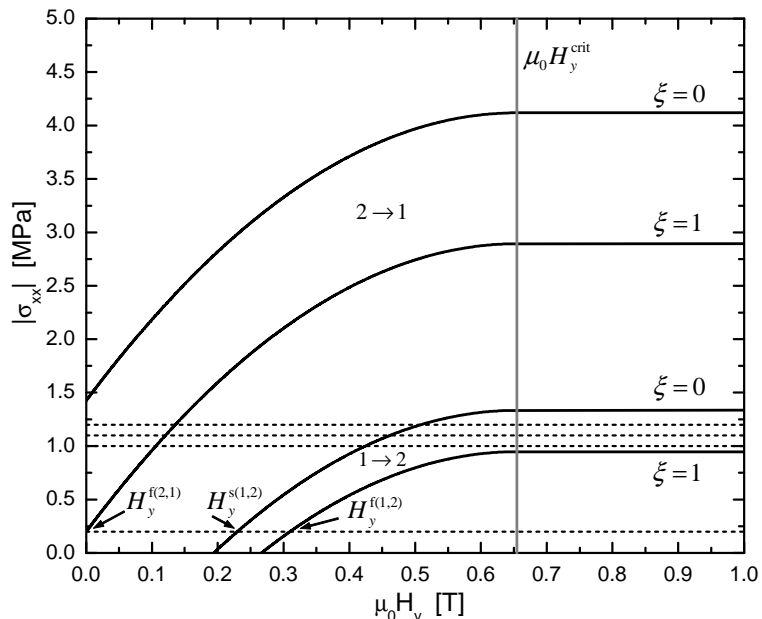
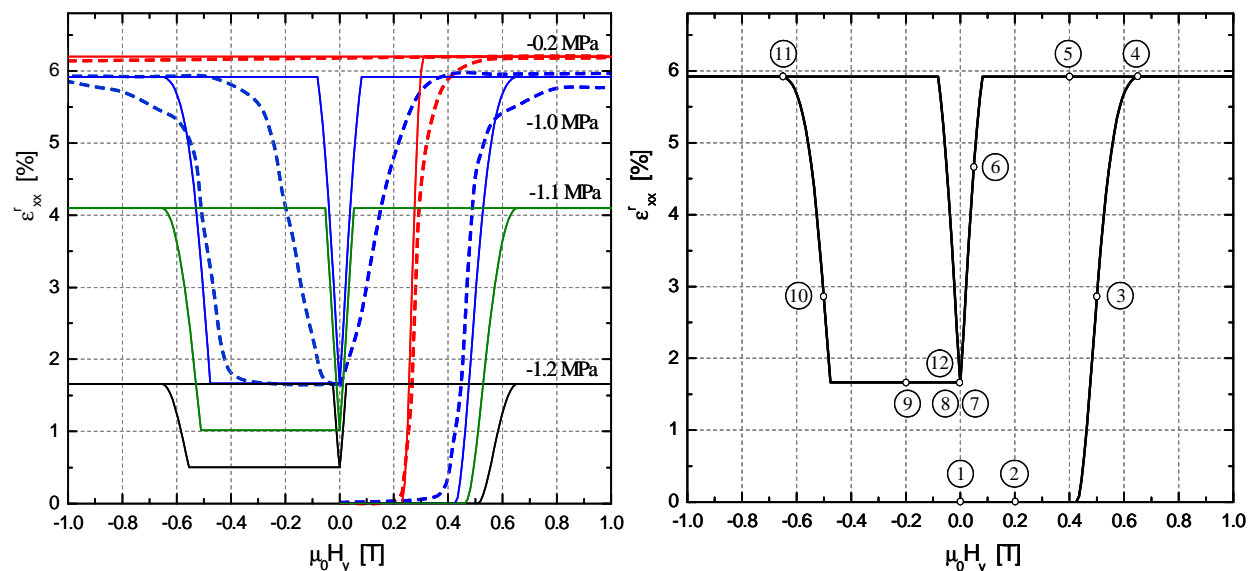


Figure 1. Numerical variant reorientation diagram in $|\sigma_{xx}|-\mu_0 H_y$ -space. Dashed lines: magnetic loading at the constant stress levels of -0.2, -1.0, -1.1 and -1.2 MPa.

the reorientation strain and not the total strain has been plotted in this figure. The curve at -0.2 MPa has to be considered a simulation, since its experimental equivalent was used to obtain the model parameters. The curves at all other stress levels, however, are model predictions. It is again emphasized, that the **same** set of parameters has been used for all of the predictions.



(a) Predicted MFIS hysteresis curves at different stress levels (solid lines) and comparison to experimental data (dashed lines).²⁵

(b) Detail: MFIS hysteresis loop under -1.0 MPa.

Figure 2. Predicted magnetic field-induced strain curves under constant stress and variable perpendicular magnetic field.

One observes that the model is capable of capturing the nonlinear and hysteretic nature of the material response. The predicted stress-dependent shape of the hysteresis curves reflects the fact that raising the stress level delays the onset and the termination of the reorientation from the stress-favored to the magnetic field-favored variant, such that higher magnetic fields are needed to initiate and complete the process. The model also predicts the reduction of the obtainable MFIS with increasing stress level and the magnitude of residual reorientation strain for each loop. The experimentally observed and predicted asymmetry of the hysteresis loop has been termed the *first cycle effect*.²⁶ Subsequent cycles are symmetric.

To explain the predicted evolution of the MFIS in more detail, figure 2(b) takes a closer look at the hysteresis loop under -1.0 MPa. Different characteristic configurations along the loading path have been numbered. For each of them table 4 shows a schematic representation of the variant volume fraction and the magnetization rotation along with listing the current values of the applied magnetic field, and the internal variables, i. e. the reorientation strain, variant volume fraction and magnetization rotation angle. It should be made clear that the configurations shown in table 4 are only schematics designed to illustrate the connection of the macroscopic behavior to the evolution of the internal state variables. They do not represent the actual distribution of the variants throughout a single crystal specimen.^d

Table 4. Configuration schematics and data for the predicted -1.0 MPa MFIS hysteresis curve.

#	Schematic	$\mu_0 H_y$	ε_{xx}^r	ξ	θ_3	#	Schematic	$\mu_0 H_y$	ε_{xx}^r	ξ	$\theta_3(\theta_1)$
1		0.0 T	0.0 %	0.0	0.0°	7		0.0 ⁺ T	1.67 %	0.27	0.0°
2		0.2 T	0.0 %	0.0	17.8°	8		0.0 ⁻ T	1.67 %	0.27	0.0°
3		0.5 T	2.84 %	0.46	49.8°	9		-0.2 T	1.67 %	0.27	17.8°
4		0.65 T	5.92 %	0.95	90.0°	10		-0.5 T	2.84 %	0.46	49.8°
5		0.4 T	5.92 %	0.95	37.7°	11		-0.65 T	5.92 %	0.95	90.0°
6		0.05 T	4.68 %	0.75	4.4°	12		0.0 ⁻ T	1.67 %	0.27	0.0°

The prediction starts with the depicted single variant, single domain configuration 1, where, as discussed, it has been assumed that the error made by neglecting the magnetic domain wall motion at low magnetic fields is small. The magnetic field of 0.2 T in configuration 2 is not sufficient to initiate the rearrangement of variants against the mechanical stress and the internal resistance to twin boundary motion. However, this field causes the magnetization vector in the first variant to rotate, by 17.8°, and thus changes the magnetization of the specimen, while keeping the reorientation strain at 0 %. By increasing the magnetic field to the critical threshold value of 0.43 T the reorientation process is initiated and variant 2 nucleates. The progress of the variant rearrangement is shown in configuration 3 at the exemplary applied field of 0.5 T. At this stage 46 % of the second variant have been produced, resulting in a MFIS of 2.84 %, while the magnetization has rotated by 49.8°.

The stress of -1.0 MPa, which favors variant 1 and therefore counteracts the reorientation process, is higher than the resistance against 90° rotation of the magnetization, as dictated by the magnetocrystalline anisotropy energy. The magnetization in variant 1 therefore aligns with the external field before the reorientation process is completed, as indicated in schematic 4. Only 95 % of variant 2 and therefore 5.92% reorientation strain can be magnetically induced at this stress level. The physical justification for this effect is given by the consideration that when the magnetization in variant 1 has completely aligned with the magnetic field the Zeeman energy difference across the twin boundary vanishes and the driving force (9) does no longer depend on the magnetic field. Thus the reorientation process is terminated prematurely. In

^dThe model assumes that at each continuum point there exists an underlying length scale at which a mixture of variants and domains is observable, and that the constitutive response is an averaged behavior at that point. Whether this assumption is fully justified for the case of single crystal specimen is still a subject of discussion.

the presented model, this mechanism explains the reduction of the maximum magnetic field-induced with increasing stress levels.

According to Eq. (8) the critical magnetic field at which the magnetization in variant 1 has fully rotated is in the limit of $\theta_3 \rightarrow \frac{\pi}{2}$ given by

$$H_y^{\text{crit}} = \frac{2\rho K_1}{\mu_0 M^{\text{sat}}} . \quad (14)$$

Note that the critical field is independent of the applied stress. The relative position of the critical field and the activation field for the forward reorientation process on the magnetic field axes determines the amount of strain produced at each stress level. As previously observed from the variant reorientation diagram in figure 1 on page 7, the magnetic field-induced strain ranges from 0 % at the blocking stress to its theoretical maximum of 6.2 % for stresses below $|\sigma|=0.95$ MPa.

When the magnetic field is subsequently decreased below H_y^{crit} , to 0.4 T in configuration 5, for example, the magnetization in variant 1 rotates back towards the magnetic easy axis but the MFIS stays constant. It must be emphasized that the activation field for the reverse reorientation process is not 0.11 T, as the variant reorientation diagram in figure 1 suggests for $\xi=1$, but rather at 0.08 T, which is the appropriate activation field for $\xi=0.95$. By further lowering the field, variant 2 is reduced to 75 % at 0.05 T in configuration 6, while the magnetization rotation angle in variant 1 continues to decrease. However, for this stress level, not all of variant 1 is recovered, even at complete removal of the magnetic field, and a residual MFIS of 1.67 % remains in configuration 7. As observable in figure 2(a) as well as the variant reorientation diagram in figure 1 on page 7, higher compressive stresses help to recover a greater amount of variant 1, whereas at compressive stress levels below 0.2 MPa none of the initial single variant 1 configuration is recovered. At zero field in configuration 7 the magnetization vectors in both variants are aligned with their respective easy axes. Since the effect of domain wall motion at low magnetic fields has been neglected, a non-zero macroscopic magnetization is predicted by the model. The corresponding magnetization curves will be discussed shortly.

As a negative magnetic field is applied, the magnetization in both variants is assumed to instantaneously switch directions as indicated in schematics 7 and 8. In configuration 9 the ratio of variants remains unchanged, but the magnetization has rotated by 17.8° . Due to the mixture of variants, the activation of the reorientation process under a negative magnetic field is slightly delayed compared to the positive field hysteresis loop, and occurs at -0.48 T, which is the appropriate activation value for $\xi = 0.27$. From this point on, cf. configurations 10 and 11, the evolution of the magnetic field-induced strain is symmetric to its positive counterpart, described above in detail. In terms of the residual strain, configuration 12 at the end of the negative loop is identical to configurations 7 and 8 at the end of the positive and beginning of the negative loop, respectively. Unless a single variant configuration is not purposely restored by temporarily raising the stress level, the reorientation strain that is obtainable in subsequent cycles is reduced to 4.25 %, which is the difference in strain between the configurations 7 (or 8, 9, 12) and 4 (or 5, 11). The reduction of the obtainable MFIS is thus limited to the first cycle and hence the term first cycle effect. It should also be clear that if the negative magnetic field had been applied first, the resulting hysteresis loop had been the mirror image of the presented one.

The strong coupling between the deformation and changes in the magnetization that are characteristic of MSMA constitutive response is made evident by considering the corresponding nonlinear magnetization hysteresis curves. According to table 1 and Eqs. (2b), (3) and (8), the magnetization component in the direction of the applied field is given by

$$M_y = \xi M^{\text{sat}} + (1 - \xi) M^{\text{sat}} \sin(\theta_3) = \xi M^{\text{sat}} + (1 - \xi) \frac{\mu_0 (M^{\text{sat}})^2}{2\rho K_1} H_y . \quad (15)$$

The magnetic field-induced magnetization curves plotted in figure 3 have been computed using Eq. (15) in addition to the same set of constitutive equations used to predict the MFIS response. All of the depicted curves represent model predictions, since the model parameters were entirely calibrated using information from experimental strain curves.

Consider in particular the magnetization curve at the applied stress of -1.0 MPa, for which the corresponding MFIS hysteresis loop has just been analyzed in detail. The configuration schematics of figure 2(b) again prove helpful to understand the connection between the evolution of the internal variables and the macroscopic material response. At low magnetic fields, when the material is in its initial single variant state, the M_y -curve represents the magnetization of variant 1 along its magnetic hard axis, which occurs via

magnetization rotation. Because only the first term in the expansion of the anisotropy energy (4) has been considered, the magnetization M_y , according to (15), has a linear dependence on H_y in this region. From Eq. (15), a slope of 1.53 T^{-1} has been calculated, a result which is in excellent agreement with the experimental data (dashed line) measured by Heczko et al.²⁵ According to Eq. (8), the magnetization rotation is independent of the applied stress and all curves coincide in this initial region. The abrupt deviation from linearity of the magnetization curves occurs when the stress-dependent critical magnetic field is reached and the variant rearrangement is initiated. The magnetization in this region changes via the mechanism of variant rearrangement as well as magnetization rotation. The influence of the variant 2 magnetization becomes more prominent as the reorientation process progresses. When the critical magnetic field for full magnetization rotation in variant 1 has been reached, the reorientation process is terminated and the material is magnetized to saturation in the direction of the applied magnetic field.

Since the forward reorientation process is not completed for this stress level, the magnetization rotation in the residual variant 1 volume fraction is reduced when the magnetic field is subsequently decreased below H^{crit} , resulting again in a linear variation of the magnetization. The slope, however, is different from the one initially observed for variant 1 at low magnetic fields, since 95 % of the material still consist of variant 2, whose magnetization remains unaffected by the decrease of the magnetic field. Another abrupt nonlinear change in the magnetization occurs when the reverse reorientation process is activated. Due to the residual variant 2 volume fraction of 27 %, a non-zero effective magnetization is predicted at zero applied field, even though the magnetization in variant 1 has rotated back to its reference configuration. The model also predicts a jump of the magnetization curve as the applied field switches sign. As discussed, this discontinuity is a direct consequence of neglecting the mechanism of domain wall motion. The prediction of magnetization curves in this region thus deviates from the experimental measurements. However, the importance of this difference has not been deemed sufficient to justify raising the level of complexity of the model by accounting for the complicated evolution of the magnetic domains. This is only necessary if the main goal is to predict the MSMA magnetization response at low magnetic fields. For actuator applications the assumption of a fixed magnetic domain structure yields sufficiently accurate predictions.

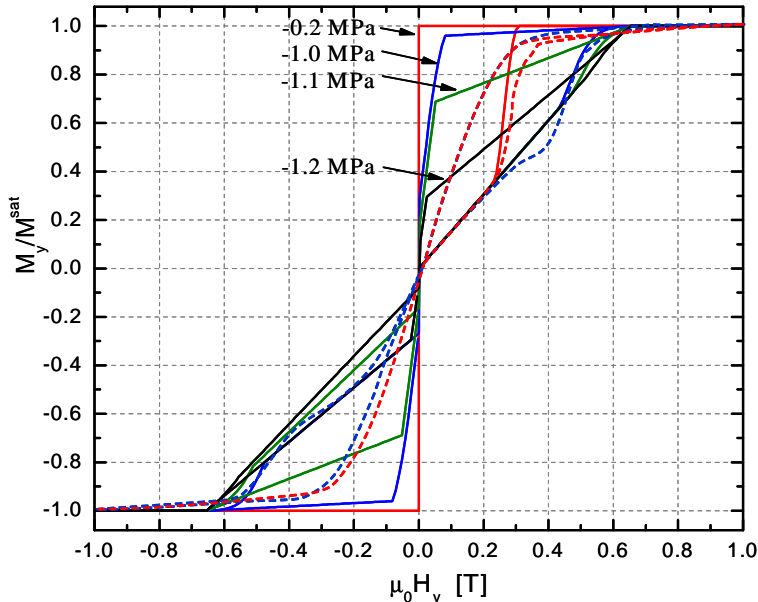


Figure 3. Predicted magnetization hysteresis curves at different stress levels (solid lines) and comparison to experimental data²⁵ (dashed lines) at the stress levels of -0.2 and -1.0 MPa.

B. Variant reorientation under a variable uniaxial stress and a constant transverse magnetic field

B. Variant reorientation under a variable uniaxial stress and a constant transverse magnetic field

A second loading case of practical interest is the reorientation of martensitic variants under mechanical loads and constant magnetic field. Such loading occurs for example when an increase in the axial compressive stress at the end of a magnetic cycle, such as one of those presented in figure 2(a) on page 7, is used to restore the initial single variant 1 configuration.

In this section it is demonstrated that the model, *without* adjustment of the model parameters, predicts the corresponding stress-strain response of the MSMA. Again the loading paths are graphically represented in the variant reorientation diagram shown in figure 4. The sequence of loading is such that first the magnetic field is raised to 1 T under the constant stress of -0.2 MPa, which is path I. The magnetic field is then lowered to different values denoted H_y^{exp} of 0.0, 0.2, 0.4, 0.6 and 0.8 T. Subsequently, the compressive stress is increased to -5 MPa (IIa–IIe) under the respective constant magnetic field, lowered back to -0.2 MPa, and

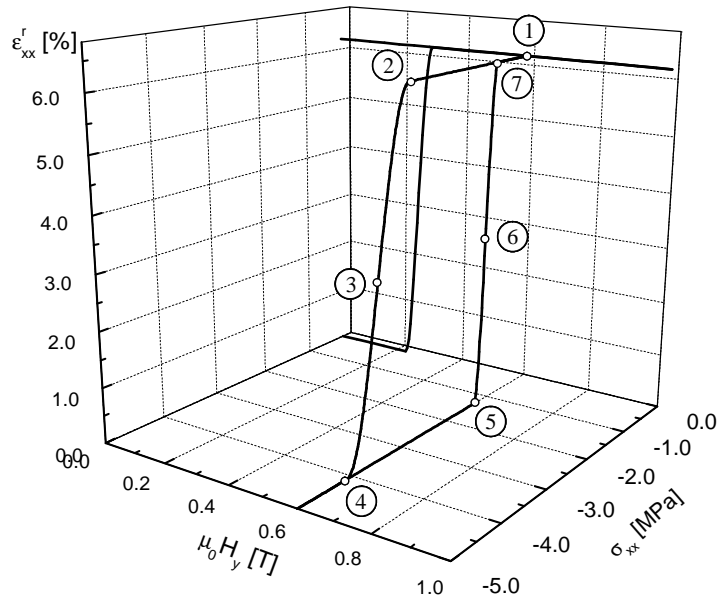









Figure 6. Detail: Stress-induced reorientation strain hysteresis loop under 0.6 T, i. e. path IIId.

of variant 2. The compressive stress completely reorients the variants, configurations 2–4, but the magnetic field is so high, that the stress-induced variant 1 configuration 4 is not sustained, but rather reversed to variant 2 as the mechanical load decreases, cf. configurations 5–7. As the magnetic field is subsequently removed, the constant stress level of -0.2 MPa is not sufficient to recover variant 1. The loading paths IIa–IIe can be explained in a similar manner.

Table 5. Configuration schematics and data for the strain hysteresis loop under 0.6 T.

#	Schematic	σ_{xx}	$\mu_0 H_y$	ε_{xx}^r	ξ	θ_3
1		-0.2 MPa	0.6 T	6.2 %	1.0	—
2		-2.87 MPa	0.6 T	6.2 %	1.0	—
3		-3.49 MPa	0.6 T	3.1 %	0.5	66.4°
4		-4.1 MPa	0.6 T	0.0 %	0.0	66.4°
5		-1.31 MPa	0.6 T	0.0 %	0.0	66.4°
6		-1.12 MPa	0.6 T	3.1 %	0.5	66.4°
7		-0.93 MPa	0.6 T	6.2 %	1.0	—

The corresponding stress-induced magnetization curves are shown in figure 7. It is interesting to note that these hysteresis loops are different in nature than the magnetic field-induced magnetization curves previously shown in figure 3 on page 10. The main reason is that, since the mechanical detwinning of variants occurs at constant magnetic fields, the magnetization vectors in each variant do not rotate. Therefore the only mechanism for changing the magnetization is the variant reorientation, whereas in the magnetic field-induced case the magnetization rotation provided an additional mechanism. Furthermore, because of the constant magnetic field, the normalized y-component of the magnetization does not reduce to zero even if the

reorientation process is complete, so that the size of the magnetization hysteresis loop is stress-dependent, whereas the same strain is induced for all loading paths. This is the opposite effect compared to that observed for the magnetic field-induced case of Section III.A.

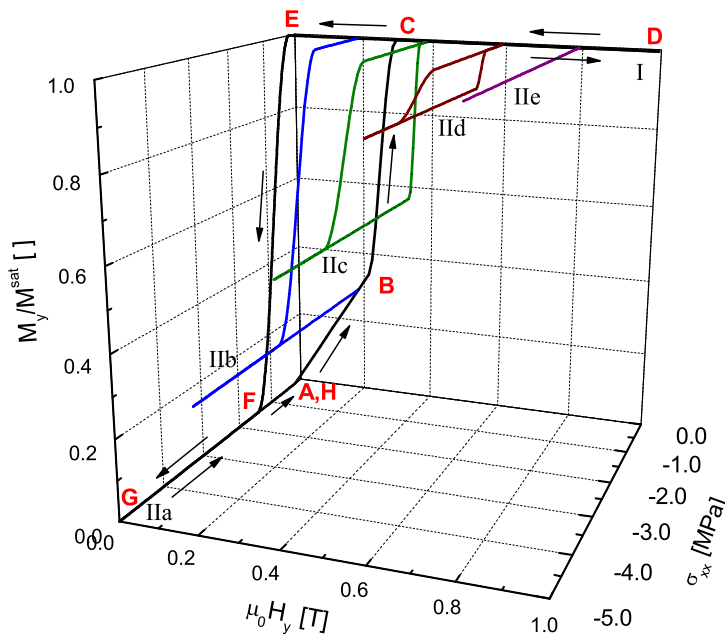


Figure 7. Normalized magnetization vs. stress and magnetic field. Initial constant stress loop at -0.2 MPa.

IV. Discussion

It has been shown that the constitutive model presented in this paper can successfully be applied to predict the strain and magnetization response of magnetic shape memory alloys under complex loading conditions. The model predictions demonstrate the potential of MSMA for applications as sensors or actuators in smart structures, where complex magnetomechanical loads are to be expected. In particular, the cases of magnetic field-induced reorientation of martensitic variants under constant stress and stress-induced reorientation under constant magnetic fields were discussed. Combinations of the above loading paths were used to demonstrate the influence of the sequence of loading on the constitutive response. Important features of the macroscopic behavior, such as the stress-dependence of the induced reorientation strain, the residual reorientation strain and the first cycle effect were explained in detail by establishing the connection to the evolution of the microstructure. It was shown that in the presented approach internal state variables account for this evolution in a phenomenological sense, thereby introducing dissipative effects into the formulation. In this manner the model predictions reflect the strong dependence of the MSMA response on the sequence of loading; a feature that can not be achieved by models that rely entirely on the minimization of the free energy.

Other interesting loading conditions that will be addressed in future modeling efforts involve multiple components of the magnetic field. The x -component of the magnetic field favors the same variant as the compressive x -component the stress and can therefore alternatively be used to recover the single variant 1 configuration. However, in this case the magnetization vectors in both variants are expected to rotate and thus the magnetization response will be different from that observed in the mechanical detwinning case.

An important aspect of modeling the MSMA response under complex loading paths is the validation of the predictions with the help of experimental data. These experiments, however, prove to be difficult to conduct and for the work presented in this publication only limited data were available. More detailed validations of the model for complex loading will be conducted in the future if the necessary data can be obtained.

In order to design reliable MSMA applications it is also inevitable that one solves appropriate magne-

tomechanical boundary problems. Even if the stress state can be assumed to be uniaxial and homogeneous, such that the mechanical equilibrium equations are satisfied, this procedure at least involves solving magnetostatic problems for specific geometries, while accounting for the MSMA constitutive response. Such problems have been addressed by the authors,²¹ and will also be the focus of future work.

Acknowledgments

This work was supported by the Army Research Office, Contract No. DAAD 19-02-1-0261, the National Science Foundation — Division of Materials Research, Contract No. 0244126, and the U.S. Civilian Research & Development Foundation, Grant No. RE1-2525-TO-03.

References

- ¹Ullakko, K., Huang, J. K., Kantner, C., O’Handley, R. C., and Kokorin, V. V., “Large Magnetic-Field-Induced Strains in Ni₂MnGa Single Crystals,” *Applied Physics Letters*, Vol. 69, No. 13, 1996, pp. 1966–1968.
- ²O’Handley, R. C., Allen, S. M., Paul, D. I., Henry, C. P., Marioni, M., Bono, D., Jenkins, C., Banful, A., and Wager, R., “Keynote Address: Magnetic Field-Induced Strain in Single Crystal Ni-Mn-Ga,” *Proceedings of SPIE, Symposium on Smart Structures and Materials*, Vol. 5053, 2003, pp. 200–206.
- ³Cui, J., Shield, T. W., and Wuttig, M., “Magnetostriction of Stress-Induced Martensite,” *Applied Physics Letters*, Vol. 85, No. 8, 2004, pp. 1–3.
- ⁴Yamamoto, T., Taya, M., Sutou, Y., Liang, Y., Wada, T., and Sorensen, L., “Magnetic Field-Induced Reversible Variant rearrangement in Fe-Pd single crystals,” *Acta Materialia*, Vol. 52, No. 17, 2004, pp. 5083–5091.
- ⁵Murray, S. J., Hayashi, R., Marioni, M., Allen, S. M., and O’Handley, R. C., “Magnetic and Mechanical Properties of FeNiCoTi and NiMnGa Magnetic Shape Memory Alloys,” *Proceedings of SPIE*, Vol. 3675, 1999, pp. 204–211.
- ⁶Karaca, H. E., Karaman, I., Chumlyakov, Y. I., Lagoudas, D. C., and Zhang, X., “Compressive Response of a Single Crystalline CoNiAl Shape Memory Alloy,” *Scripta Materialia*, Vol. 51, 2004, pp. 261–266.
- ⁷Pasquale, M., “Mechanical Sensors and Actuators,” *Sensors and Actuators A*, Vol. 106, 2003, pp. 142–148.
- ⁸Tellinen, J., Suorsa, I., Jääskeläinen, Aaltio, I., and Ullakko, K., “Basic Properties of Magnetic Shape Memory Actuators,” *Proceedings of the 8th International Conference ACTUATOR 2002, Bremen, Germany, 10-12 June 2002*, 2002, pp. 566–569.
- ⁹Chopra, I., “Status of application of smart structures technology to rotorcraft systems,” *American Helicopter Society, Journal (0002-8711)*, Vol. 45, No. 4, 2000, pp. 228–252.
- ¹⁰Chopra, I., “Review of State of Art of Smart Structures and Integrated Systems,” *AIAA Journal*, Vol. 40, No. 11, 2002, pp. 2145–2187.
- ¹¹Strelec, J. K., Lagoudas, D. C., Khan, M. A., and Yen, J., “Design and Implementation of a Shape Memory Alloy Actuated Reconfigurable Wing,” *Journal of Intelligent Material Systems and Structures*, Vol. 14, 2003, pp. 257–273.
- ¹²AdaptaMat Ltd., “MSM Actuators,” www.adaptamat.com, 2005.
- ¹³O’Handley, R. C., “Model for Strain and Magnetization in Magnetic Shape-Memory Alloys,” *Journal of Applied Physics*, Vol. 83, No. 6, 1998, pp. 3263–3270.
- ¹⁴James, R. D. and Hane, K. F., “Martensitic Transformations and Shape-Memory Materials,” *Acta Materialia*, Vol. 48, No. 1, 2000, pp. 197–222.
- ¹⁵Hirsinger, L. and Lexcellent, C., “Modelling Detwinning of Martensite Platelets Under Magnetic and (or) Stress Actions on NiMnGa Alloys,” *Journal of Magnetism and Magnetic Materials*, Vol. 254–255, 2003, pp. 275–277.
- ¹⁶Hirsinger, L. and Lexcellent, C., “Internal Variable Model for Magneto-Mechanical Behaviour of Ferromagnetic Shape Memory Alloys Ni-Mn-Ga,” *Journal de Physique IV France*, Vol. 112, 2003, pp. 977–980.
- ¹⁷Shield, T. W., “Magnetomechanical Testing Machine for Ferromagnetic Shape-Memory Alloys,” *Review of Scientific Instruments*, Vol. 74, No. 9, 2003, pp. 4077–4088.
- ¹⁸Kiefer, B. and Lagoudas, D. C., “Phenomenological Modeling of Ferromagnetic Shape Memory Alloys,” *Proceedings of SPIE, Smart Structures and Materials: Active Materials: Behavior and Mechanics, San Diego, CA, 14–18 March 2004*, Vol. 5387, 2004, pp. 164–176.
- ¹⁹Kiefer, B. and Lagoudas, D. C., “Magnetic Field-Induced Martensitic Variant Reorientation in Magnetic Shape Memory Alloys,” *Philosophical Magazine Special Issue: Recent Advances in Theoretical Mechanics, in Honor of SES 2003 A.C. Eringen Medalist G.A. Maugin*, Vol. 85, No. 33-35, 2005, pp. 4289–4329.
- ²⁰Kiefer, B. and Lagoudas, D. C., “Modeling of the Magnetic Field-Induced Martensitic Variant Reorientation and the Associated Magnetic Shape Memory Effect in MSMAs,” *Proceedings of SPIE, Smart Structures and Materials: Active Materials: Behavior and Mechanics, San Diego, CA, 6–10 March 2005*, Vol. 5761, 2005, pp. 454–465.
- ²¹Kiefer, B. and Lagoudas, D., “Application of a Magnetic SMA Constitutive Model in the Analysis of Magnetomechanical Boundary Value Problems,” *Proceedings of SPIE, Smart Structures and Materials: Active Materials: Behavior and Mechanics, San Diego, CA, 26 February–2 March 2006*, Vol. 6170, 2006.
- ²²Lagoudas, D. C., Entchev, P. B., Popov, P., Patoor, E., Brinson, L. C., and Gao, X., “Shape Memory Alloys, Part II: Modeling of Polycrystals,” *Mechanics of Materials*, Vol. 38, No. 5–6, 2006, pp. 430–462.
- ²³Patoor, E., Lagoudas, D. C., Entchev, P. B., Brinson, L. C., and Gao, X., “Shape Memory Alloys, Part I: General Properties and Modeling of Single Crystals,” *Mechanics of Materials*, Vol. 38, No. 5–6, 2006, pp. 391–429.
- ²⁴Hirsinger, L., Creton, N., and Lexcellent, C., “From Crystallographic Properties to Macroscopic Detwinning Strain and Magnetisation of Ni-Mn-Ga Magnetic Shape Memory Alloys,” *Journal de Physique IV France*, Vol. 115, 2004, pp. 111–120.

- ²⁵Heczko, O., Straka, L., and Ullakko, K., "Relation Between Structure, Magnetization Process and Magnetic Shape Memory Effect of Various Martensites Occuring in Ni-Mn-Ga alloys," *Journal de Physique IV France*, Vol. 112, 2003, pp. 959–962.
- ²⁶Kiefer, B., Karaca, H. E., Lagoudas, D. C., and Karaman, I., "Characterization and Modeling of the Magnetic Field-Induced Strain and Work Output in Ni₂MnGa Shape Memory Alloys," *Submitted to Journal of Magnetism and Magnetic Materials*, 2005.
- ²⁷Straka, L. and Heczko, O., "Reversible 6% Strain of Ni-Mn-Ga Martensite Using Opposing External Stress in Static and Variable Magnetic Fields," *Journal of Magnetism and Magnetic Materials*, Vol. 290–291, 2005, pp. 829–831.
- ²⁸Karaca, H. E., Karaman, I., Basaran, B., Chumlyakov, Y. I., and Maier, H. J., "Magnetic Field and Stress Induced Martensite Reorientation in NiMnGa Ferromagnetic Shape Memory Alloy Single Crystals," *Acta Materialia*, Vol. 54, No. 1, 2006, pp. 233–245.
- ²⁹Coleman, B. D. and Noll, W., "The Thermodynamics of Elastic Materials with Heat Conduction and Viscosity," *Archive for Rational Mechanics and Analysis*, Vol. 13, 1963, pp. 167–178.
- ³⁰Coleman, B. D. and Gurtin, M. E., "Thermodynamics with Internal State Variables," *The Journal of Chemical Physics*, Vol. 47, No. 2, July 1967, pp. 597–613.
- ³¹Heczko, O., "Magnetic Shape Memory Effect and Magnetization Reversal," *Journal of Magnetism and Magnetic Materials*, Vol. 290–291, No. 2, 2005, pp. 787–794.
- ³²Sullivan, M. R. and Chopra, H. D., "Temperature- and Field-Dependent Evolution of Micromagnetic Structure in Ferromagnetic Shape-Memory-Alloys," *Physical Review B*, Vol. 70, 2004, pp. 094427–(1–8).
- ³³O'Handley, R. C., *Modern Magnetic Materials*, John Wiley & Sons, 2000.
- ³⁴Jin, Y. M., Wang, Y. U., Kazaryan, A., Wang, Y., Laughlin, D. E., and Khachaturyan, A. G., "Magnetic Structure and Hysteresis in Hard Magnetic Nanocrystalline Film: Computer Simulation," *Journal of Applied Physics*, Vol. 92, No. 10, 2002, pp. 6172–6181.
- ³⁵Cullity, B. D., *Introduction to Magnetic Materials*, Addison-Wesley, 1972.
- ³⁶Kittel, C., *Introduction to Solid State Physics*, John Wiley & Sons, 7th ed., 1996.
- ³⁷Kittel, C., "Physical Theory of Ferromagnetic Domains," *Reviews of Modern Physics*, Vol. 21, No. 4, 1949, pp. 541–583.
- ³⁸Tickle, R., *Ferromagnetic Shape Memory Materials*, Ph.D. thesis, University of Minnesota, May 2000.
- ³⁹James, R. D. and Wuttig, M., "Magnetostriction of Martensite," *Philosophical Magazine A*, Vol. 77, No. 5, 1998, pp. 1273–1299.
- ⁴⁰Heczko, O. and Straka, L., "Compositional Dependence of Structure, Magnetization and Magnetic Anisotropy in Ni-Mn-Ga Magnetic Shape Memory Alloys," *Journal of Magnetism and Magnetic Materials*, Vol. 272–276, No. Part 3, 2004, pp. 2045–2046.
- ⁴¹Lagoudas, D. C., Bo, Z., and Qidwai, M. A., "A Unified Thermodynamic Constitutive Model for SMA and Finite Element Analysis of Active Metal Matrix Composites," *Mechanics of Composite Materials and Structures*, Vol. 3, 1996, pp. 153–179.
- ⁴²Bekker, A. and Brinson, L. C., "Phase Diagram Based Description of the Hysteresis Behavior of Shape Memory Alloys," *Acta Materialia*, Vol. 46, No. 10, 1998, pp. 3649–3665.